ARTICLE Communicated by Dan Tranchina

A Population Study of Integrate-and-Fire-or-Burst Neurons

A.R.R. Casti
arc@camelot.mssm.edu
A. Omurtag
ahmet@camelot.mssm.edu
A. Sornborger
ats@camelot.mssm.edu
Laboratory of Applied Mathematics, Mount Sinai School of Medicine, New York, NY 10029, U.S.A.

E. Kaplan
kaplane@mail.rockefeller.edu
Laboratory of Applied Mathematics and Department of Ophthalmology, Mount Sinai School of Medicine, New York, NY 10029, U.S.A.

B. Knight
knight@rockvax.rockefeller.edu
Laboratory of Applied Mathematics, Mount Sinai School of Medicine, New York, NY 10029, U.S.A.

J. Victor
jdvicto@med.cornell.edu
Department of Neurology and Neuroscience, Weill Medical College of Cornell University, New York, NY 10021, U.S.A.

L. Sirovich
chico@camelot.mssm.edu
Laboratory of Applied Mathematics, Mount Sinai School of Medicine, New York, NY 10029, U.S.A.

Any realistic model of the neuronal pathway from the retina to the visual cortex (V1) must account for the bursting behavior of neurons in the lateral geniculate nucleus (LGN). A robust but minimal model, the integrate-and-fire-or-burst (IFB) model, has recently been proposed for individual LGN neurons. Based on this, we derive a dynamic population model and study a population of such LGN cells. This population model, the first simulation of its kind evolving in a two-dimensional phase space, is used to study the behavior of bursting populations in response to diverse stimulus conditions.

1 Introduction

The lateral geniculate nucleus (LGN) is the main gateway to the visual cortex. Unlike the receptive fields of cortical neurons, the receptive fields of LGN relay cells have essentially the same center-surround structure as their retinal afferents. This observation, coupled with the roughly equal numbers of retinal ganglion cells and LGN cells, led to the view that the LGN is a passive relay that simply transmits a faithful replica of the input to the cortex. Anatomical data, however, show that retinal afferents comprise just 10% to 20% of the input to the LGN (Sherman & Guillery, 1996). The majority of LGN input originates in the cortex and parabrachial region of the brainstem, with some inhibitory contributions coming from local interneurons and from cells of the thalamic reticular nucleus, neither of which makes direct connections with higher levels in the visual pathway. This complex connectivity implies that the LGN serves as more than a passive relay.

Further evidence of the LGN's active role in visual processing is the dual modality of its so-called relay cells. When sufficiently depolarized, an LGN cell will fire in a tonic mode, characterized by a train of regularly spaced spikes, with a nearly linear response over a range of time-dependent stimuli that typify real-world input (0–10 Hz) (Mukherjee & Kaplan, 1998). In tonic mode, relay cells are well modeled by classic integrate-and-fire dynamics (Tuckwell, 1988). Because of the primarily linear input-output relationship when an LGN neuron fires in tonic mode, this state imparts to the cortex a relatively faithful rendition of the visual stimulus over the entire duration in which it is coded by the retinal ganglion cells.

Relay cells may also respond in a distinctly different mode, the burst mode, in which a cell fires bursts of 2 to 10 spikes, with an interspike interval of about 4 ms or less (Guido, Lu, & Sherman, 1992), followed by a refractory period on the order of 100 ms before the next burst. Burst behavior is precipitated by a low-threshold calcium spike that occurs when the cell is hyperpolarized sufficiently to deinactivate calcium T-channels (Jahnsen & Llinas, 1982). The calcium spike is termed low threshold because it is initiated at much more negative membrane potentials than those that initiate conventional spikes that are mediated by activated sodium and potassium channels. After its deinactivation, the calcium channels may be activated by current injection or depolarizing excitatory postsynaptic potentials. If the cell is driven past threshold, it then fires a train of action potentials for about 20 to 50 ms until the T-channels inactivate, after which the burst cycle begins anew, provided the cell is again hyperpolarized below the deinactivation threshold. The burst mode is a nonlinear response since it is intermittent, whether driven by continuous or steplike input. Further, because of the all-or-none character of the low-threshold calcium spike, the dynamics of burst response is essentially the same in both amplitude and the number of spikes, regardless of whether the cell is driven just above its firing threshold or well past it. Thus, in contrast to the transmission of visual input in tonic

mode, the LGN in burst mode transmits a modified version of the visual stimulus to the cortex. The time dependence of the input and differences in driving strength appear to have little influence on the details of the burst activity, which is shaped primarily by the intrinsic dynamics of the relay neuron.

The functional significance of the LGN's two distinct modes of operation may be related to attentional demands. Relay cells of fully awake animals tend to fire in tonic mode, which suggests that a faithful transmission of retinal activity is the primary need of the alert animal. Rhythmic bursting, on the other hand, is common for low arousal states (Livingstone & Hubel, 1981) and during paroxsymal events such as epileptic seizures (Steriade & Contreras, 1995). Arrhythmic bursting has been observed (Guido & Weyand, 1995) in both lightly anaesthetized and fully awake cats subjected to a visual stimulus. Taken together, these results indicate that the burst mode is not solely associated with a sleep state or functional disorders, and the variability of bursting patterns may signal distinct events to the cortex.

Another difference between the tonic and burst modes is their temporal frequency response (Mukherjee & Kaplan, 1995). Relatively depolarized cells, which fire in tonic mode when stimulated, act as low-pass filters. The transfer function of bursting cells, on the other hand, has a low-frequency cutoff. Because real-world stimuli typically contain low frequencies, the implication is that the job of the tonic mode is to transmit more faithfully the details of synaptic events responding to a specific visual stimulus. Sudden changes in retinal input, however, have more power at high frequencies, so the role of the burst mode may be to disable the geniculate relay and tell the cortex that nothing is happening when bursting rhythmically, but to signal sharp changes in the visual field with arrhythmic bursts. Furthermore, there is evidence that the LGN switches between burst and tonic mode depending on the attentional needs of higher levels of the visual pathway (Sherman, 1996). This hypothesis provides a potential explanation for the intricate feedback connections arriving from the cortex and the brainstem, a connectivity pattern that is likely not accidental.

Clearly, any realistic model of the visual pathway must account for the dual behavior of the LGN. In this work, we elaborate on the features of a recent detailed model (Smith, Cox, Sherman, & Rinzel, 2000) of thalamic relay cells. Our principal purpose is to demonstrate the utility of a particular approach, the population dynamics method, in the simulation of a population of LGN cells that accurately mirrors the burst and tonic modes over a wide range of stimulus conditions. Although it is well known that the discharge of individual LGN neurons can be tightly correlated with the activity of individual retinal ganglion cells (Troy & Robson, 1992), this aspect of the physiology will not be considered, and the input to an LGN cell, at least implicitly, will be modeled by Poisson arrivals. We consider the behavior of an assembly of LGN cells in the same spirit in which Smith et al. (2000) consider individual LGN neuron responses to external driving.

The population method presented here illustrates a higher-dimensional extension of previous models (Knight, 1972; Knight, Manin, & Sirovich, 1996; Knight, Omurtag, & Sirovich, 2000; Nykamp & Tranchina, 2000; Omurtag, Knight, & Sirovich, 2000; Sirovich, Knight, & Omurtag, 2000) used in the simulation of a population of integrate-and-fire cells. A model with an additional underlying dimension is necessary to capture the dependence of relay cells on the calcium channel conductance, or on any other ion channels that may be operative. To illustrate the population method for relay cells, we employ a two-dimensional state space model for individual LGN cells as suggested by Smith et al. (2000). In section 2, we review this single-cell model and formulate the corresponding population equation. In section 3, we present simulations of a population driven by steady and step input currents and compare the validity of these results against a direct simulation of 10^4 neurons, each of which follows the integrate-and-fire-or-burst dynamics. The appendix contains the details of the numerical techniques used.

2 Integrate-and-Fire-or-Burst Population Equations

Smith et al. (2000) have presented a model of relay neurons in the LGN of a cat. Their model extends the classic integrate-and-fire dynamics to a two-dimensional system that involves a membrane voltage, V, and a gating variable, h, which models a slow Ca^{2+} current. The slow current, usually referred to as the T-channel current, allows bursts of impulses to be fired by a cell which recovers from hyperpolarization (Jahnsen & Llinas, 1982). Thalamic cells that are sufficiently depolarized (roughly $V > -60\,\text{mV}$) do not burst, but exhibit integrate-and-fire behavior when a depolarizing current is applied. Both of these features are built into the integrate-and-fire-or-burst (IFB) model that we use to model the activity of each neuron of a population. After a brief review of the single-cell equations, we derive the kinetic equation for a population of IFB cells.

2.1 Dynamical Equations for an IFB Neuron. The IFB model introduced in Smith et al. (2000) includes a Hodgkin-Huxley type equation for the voltage V,

$$C\frac{dV}{dt} = I - I_L - I_T. \tag{2.1}$$

Here, I is an applied current, I_L is a leakage current of the form

$$I_L = g_L(V - V_L), \tag{2.2}$$

and the current I_T couples the dynamics of V to the calcium conductance variable h,

$$I_T = g_T m_\infty h(V - V_T), \tag{2.3}$$

where $m_\infty(V)$ is an activation function for the Ca^{2+} channel, and V_L and V_T are the reversal potentials for the leakage and calcium ions. For simplicity, m_∞ is represented as a Heaviside function:

$$m_\infty(V) = H(V - V_h) = \begin{cases} 1 & (V > V_h) \\ 0 & (V < V_h). \end{cases} \tag{2.4}$$

The dynamics of the Ca^{2+} current, which typically varies on long timescales relative to the time course of a fast sodium spike ($\leq$ 4 ms), is given in the IFB model by

$$\frac{dh}{dt} = \begin{cases} -\dfrac{h}{\tau_h^-} & (V > V_h) \\ \dfrac{1-h}{\tau_h^+} & (V < V_h), \end{cases} \tag{2.5}$$

so h always approaches either zero or one. The parameter V_h divides the V axis into a hyperpolarizing region ($V < V_h$), where the calcium current is deinactivated, and a nonhyperpolarizing region ($V > V_h$) in which the calcium current is inactivated. The timescale τ_h^- sets the duration of a burst event, and τ_h^+ controls the inactivation rate. In accordance with the literature, $\tau_h^+ \gg \tau_h^-$ (Smith et al., 2000).

The leakage reversal potential V_L (≈ -65 mV) sets the rest voltage in the absence of a stimulus, and for mammalian LGN cells in vitro, V_L typically lies below the potential V_h (≈ -60mV) at which burst behavior is observed (Jahnsen & Llinas, 1982). The reversal potential V_T ($\approx$ 120 mV) for the calcium ions is relatively large and causes rapid depolarization once the T-channels are activated. On crossing the firing-threshold voltage, $V_\theta \approx -35$ mV, the cell fires and the membrane potential is reset to $V_r > V_h$, where $V_r \approx -50$ mV is typical. Consequently, the five voltage parameters of the IFB model satisfy the relation

$$V_L < V_h < V_r < V_\theta < V_T. \tag{2.6}$$

The calcium variable h ranges between 0 and 1. For relatively large values of h, a cell will burst due to the calcium channel coupling term and will produce fast trajectories in V with rapid resets. For relatively low values of h, given a large enough input current, tonic firing occurs. Figure 1 illustrates these dynamic features of the IFB model. In this simulation, the neuron was driven by Poisson-distributed synaptic events that increased the membrane potential by $\epsilon = 1.5$ mV with each occurrence. The driving rate was chosen too small for the cell to fire in tonic mode. Instead, the cell drifted randomly near the threshold $V_h = -60$ mV for Ca^{2+} deinactivation. Bursts occurred

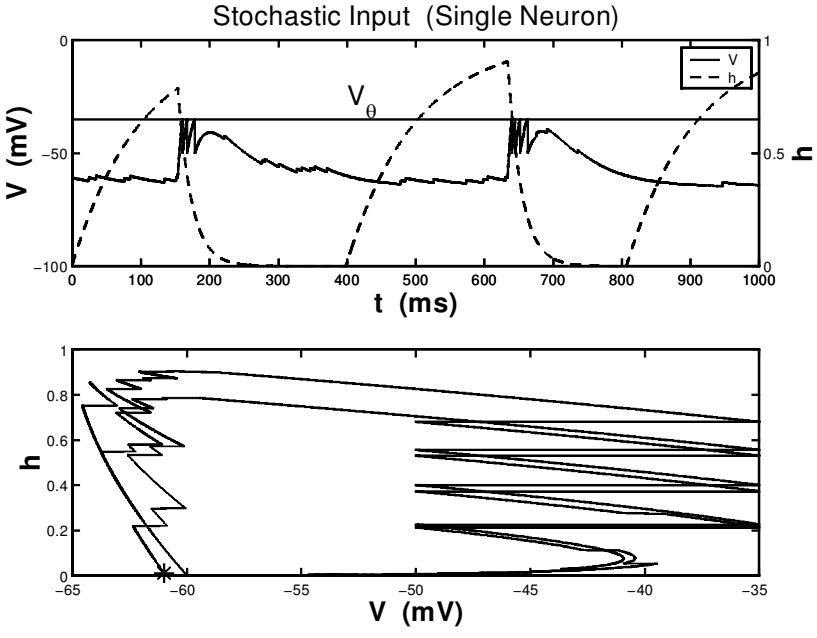

Figure 1: Simulation of a single IFB neuron driven by Poisson-distributed synaptic events with fixed mean arrival rate $\sigma^0 = \frac{I}{C\epsilon}$, with $I = .08\,\frac{\mu A}{cm^2}$, $\epsilon = 1.5\,\text{mV}$, and all other parameters as in Table 1. (Top) Time series for V (solid line) and h (dashed line). The horizontal line demarcates the threshold $V = V_\theta$. (Bottom) Phase plane orbit. The asterisk locates the initial condition $(V_0, h_0) = (-61, .01)$. In the time span shown, there were two burst events, the first of containing three spikes and the other four spikes.

whenever the calcium channel deinactivated and enough clustered synaptic events, in collaboration with the T-channel current, conspired to drive the neuron past the firing threshold.

2.2 Population Dynamics. Our aim is to study the behavior of a population of excitatory IFB neurons. A general approach to this problem, in the limit of a continuous distribution of neurons, is presented in Knight et al. (1996), Knight (2000), Nykamp and Tranchina (2000), and Omurtag, Knight, et al. (2000). Based on the development in the cited references, the number of neurons in a state $\mathbf{v} = (V, h)$ at time t is described by a probability density, $\rho(V, h, t)$, whose dynamics respects conservation of probability. The evolution equation for ρ thus takes the form of a conservation law,

$$\frac{\partial \rho}{\partial t} = -\frac{\partial}{\partial \mathbf{v}} \cdot \mathbf{J}. \tag{2.7}$$

The probability flux,

$$\mathbf{J} = \mathbf{J}_S + \mathbf{J}_\sigma \equiv (J^V, J^h), \tag{2.8}$$

is split into two parts. The first part is a streaming flux,

$$\mathbf{J}_S = \mathbf{F}(\mathbf{v})\rho, \tag{2.9}$$

due to the direction field of the single-neuron dynamical system, equations 2.1 through 2.5, where

$$\begin{aligned}\mathbf{F}(\mathbf{v}) &= \left(-C^{-1}\left[I_L + I_T\right], \frac{(1-h)}{\tau_h^+}H(V_h - V) - \frac{h}{\tau_h^-}H(V - V_h)\right) \\ &\equiv (F^V, F^h).\end{aligned} \tag{2.10}$$

The applied current enters our analysis as a stochastic arrival term in equation 2.7, with an arrival rate $\sigma(t)$, so that each arrival elevates the membrane voltage by an increment ϵ. Written in terms of an excitation flux, this is expressed as

$$\mathbf{J}_\sigma = \hat{\mathbf{e}}_V\, \sigma(t) \int_{V-\epsilon}^{V} \rho(\tilde{V}, h, t)\, d\tilde{V}\,, \tag{2.11}$$

where $\hat{\mathbf{e}}_V$ is a unit vector pointing along the voltage direction in the (V, h) phase space. This states that the probability current in the voltage direction, across the voltage V, comes from all population members whose voltages range below V by an amount not exceeding the jump voltage ϵ. The assumptions underlying equation 2.11 are detailed in Omurtag, Knight, and Sirovich (2000).

With the flux definitions 2.9 and 2.11, the population density $\rho(V, h, t)$ evolves according to

$$\frac{\partial \rho}{\partial t} = -\frac{\partial}{\partial \mathbf{v}} \cdot [\mathbf{F}(\mathbf{v})\rho] - \sigma(t)\left[\rho(V, h, t) - \rho(V - \epsilon, h, t)\right]. \tag{2.12}$$

Although a realistic synaptic arrival initiates a continuous conductance change, this effect is well approximated by a jump of size ϵ in the membrane potential. Thus, we see in equation 2.12 a loss term proportional to $\rho(V, h, t)$ and a gain term proportional to $\rho(V - \epsilon, h, t)$ due to synaptic events. Hereafter, this is referred to as the *finite-jump model*. For purposes of exposition, we restrict attention to excitatory current inputs.

We note that (like Smith et al., 2000) we are investigating the dynamics of the thalamic cell alone, and not the integrated dynamics of the retinal ganglion cell and LGN cell pair. This involves one simplifying departure

from the actual physiological situation. For the input current I, Smith et al. (2000) use a specified smooth function of time. Our population equation 2.12 goes a bit further by including the stochastic nature of synaptic arrivals, which are treated as uncorrelated with LGN cell activity. This should be in fair accord with the physiology for nonretinal input that is many-to-one but is only an earliest approximation for the one-to-one retinal input.

2.3 Population Firing Rate. A response variable of interest is the average firing rate of individual neurons in the population, $r(t)$. In general, two input sources drive any cell of a particular population: synaptic events arriving at a rate $\sigma^0(t)$ that arise from the external neural input and synaptic events resulting from feedback within the population. We will ignore feedback in the interest of simplicity and take the input to be purely of external origin (see Omurtag, Knight, and Sirovich, 2000, for the more general treatment). The population will be assumed homogeneous, so that each neuron is driven equally at the input rate $\sigma = \sigma^0(t)$. In the case of stochastic external input, $\sigma^0(t)$ is the ensemble mean arrival rate of external nerve impulses,

$$\sigma^0(t) = \lim_{\Delta t \downarrow 0} \left\langle \frac{1}{\Delta t} \int_t^{t+\Delta t} dt \sum_{n=1}^{\infty} \delta(t - t_n^0) \right\rangle, \tag{2.13}$$

where $\delta(t)$ is the Dirac delta function, $\langle \cdot \rangle$ denotes an ensemble average, and $\{t_n^0\}_{n=1}^{\infty}$ is a set of spike arrival times.

The population firing rate, $r(t)$, is determined by the rate at which cells cross the threshold V_θ. This may be expressed as a function of the voltage-direction flux at threshold integrated over all calcium channel activation states h,

$$\begin{aligned} r(t) &= \int_0^1 dh\, J^V\left(V_\theta, h, t\right) \\ &= \int_0^1 dh\, F^V(V_\theta, h)\rho(V_\theta, h, t) + \sigma^0(t) \int_0^1 \int_{V_\theta - \epsilon}^{V_\theta} dh\, d\tilde{V}\, \rho(\tilde{V}, h, t)\,. \end{aligned} \tag{2.14}$$

2.4 Boundary Conditions. Boundary conditions on ρ are chosen to conserve total probability over the phase-space domain $\mathcal{D}$,

$$\int_{\mathcal{D}} \rho(\mathbf{v}, t)\, d\mathbf{v} = 1\,. \tag{2.15}$$

From equation 2.7 and an application of the divergence theorem, it follows that the boundary flux integrates to zero,

$$\oint_{\partial\mathcal{D}} \hat{\mathbf{n}} \cdot \mathbf{J}\, dS = 0\,, \tag{2.16}$$

where $\hat{\mathbf{n}}$ is a boundary normal vector. Our domain of interest is the box $\mathcal{D} = \{V_L \le V \le V_\theta\,,\ 0 \le h \le 1\}$, for which it is appropriate to choose the no-flux boundary conditions

$$\hat{\mathbf{n}} \cdot \mathbf{J} = 0 \quad \text{at} \quad V = V_L\,,\ h = 0, 1\,, \tag{2.17}$$

so that the outward flux vanishes at each boundary face except at the threshold boundary $V = V_\theta$. To handle the voltage offset term, $\rho(V - \epsilon, h, t)$, in the population equation 2.12, which requires evaluation of the density at points outside the box, it is natural to choose ρ to vanish at all points outside $\mathcal{D}$, and we set

$$\rho(\mathbf{v}, t) = 0\,,\ \ V \notin \mathcal{D}\,. \tag{2.18}$$

In addition, there is a reset condition that reintroduces the flux at $V = V_\theta$ back into the domain at the reset $V = V_r$. This may be incorporated directly into the population equation 2.7 by means of a delta function,

$$\frac{\partial \rho}{\partial t} = -\frac{\partial}{\partial \mathbf{v}} \cdot \mathbf{J} + J^V(V_\theta, h, t)\,\delta(V - V_r)\,. \tag{2.19}$$

It is worth noting that the threshold flux is reset pointwise in h. This is consistent with the slow temporal variation of the calcium channel, and we assume that h does not change appreciably during the time between a cell firing a spike and its subsequent fast relaxation to reset. Under these conditions, with the total flux $\mathbf{J}$ suitably redefined to include the delta function source, probability is conserved and equation 2.16 is satisfied. Equation 2.19, with the boundary conditions 2.17 and 2.18, forms the complete mathematical specification of the model for a single population.

2.5 Diffusion Approximation. An approximation that lends itself to simpler analysis is the small-jump limit, $\epsilon \to 0$. Upon expanding the density, ρ, in the excitation flux equation 2.11 through second-order terms, one obtains

$$\rho(\tilde{V}, h, t) = \rho(V, h, t) + \delta V \frac{\partial \rho}{\partial V}(V, h, t) + \mathcal{O}(\delta V^2) \quad (\tilde{V} = V + \delta V) \tag{2.20}$$

$$\begin{aligned} \mathbf{e}_V \cdot \mathbf{J}_\sigma &= \int_{-\epsilon}^{0} \left[\rho(V, h, t) + \delta V \frac{\partial \rho}{\partial V}(V, h, t) + \ldots\right] d(\delta V) \\ &\approx \epsilon \rho(V, h, t) - \frac{\epsilon^2}{2} \frac{\partial \rho}{\partial V}(V, h, t). \end{aligned} \tag{2.21}$$

Substitution of equation 2.21 into 2.7 gives the diffusion approximation (the Fokker-Planck equation),

$$\frac{\partial \rho}{\partial t} = -\frac{\partial}{\partial \mathbf{v}} \cdot (\mathbf{F} + \sigma\epsilon\, \mathbf{e}_V)\,\rho + \frac{\sigma\epsilon^2}{2} \frac{\partial^2 \rho}{\partial V^2} + J^V\left(V_\theta, h, t\right)\delta(V - V_r)\,, \tag{2.22}$$

Table 1: Model Parameters.

τ_h^-	2×10^{-2} sec
τ_h^+	10^{-1} sec
g_L	3.5×10^{-2} mS/cm^2
g_T	7×10^{-2} mS/cm^2
V_T	120 mV
V_L	−65 mV
V_θ	−35 mV
V_r	−50 mV
V_h	−60 mV
C	$2\,\mu$F/cm^2

where the approximate threshold flux is

$$J^V\left(V_\theta, h, t\right) = [F^V\left(V_\theta, h\right) + \sigma\epsilon]\rho\left(V_\theta, h, t\right) - \frac{\sigma\epsilon^2}{2}\frac{\partial\rho}{\partial V}\left(V_\theta, h, t\right). \qquad (2.23)$$

The diffusion approximation is also useful for comparison with the finite-jump model, and this will be done in section 3.2 (also see Sirovich et al., 2000).

A further simplification of the diffusion approximation is valid in the $\epsilon \to 0$ limit with $\sigma\epsilon$ finite. This special limit reduces equation 2.22 to a pure advection equation for which exact solutions can be derived (see section 3.1). Physically, this approximation is appropriate when input spike rates are extremely large and the evoked postsynaptic potentials are small. This would be the case, for example, when DC input overwhelms stochastic fluctuations.

3 Results

In Table 1 we show the parameter values used in our simulations, following Smith et al. (2000), whose choices are based on experimental data from cat LGN cells. In particular, when the cell is in burst mode, the parameter subspace near these values produces 2 to 10 spikes per burst.

We tested the population simulation with a variety of external inputs. In all cases, we compared the accuracy against a direct numerical simulation (DNS), in which equations 2.1 and 2.5 were numerically integrated for a discrete network of 10^4 neurons, each driven by Poisson-distributed action potentials involving the same voltage elevation, ϵ, with the same mean arrival rate, σ^0, as in the population simulation.

As explained in the appendix, a population simulation is sensitive to finite grid effects that do not affect the DNS, and for this reason we treat the DNS as the standard for comparison. As in Omurtag, Knight, and Sirovich (2000), the two approaches converge for a sufficiently fine mesh. For instance, as seen in Figure 6, the firing-rate response curve to a step input current generated by the DNS overshoots the converged mean firing rate of

the population simulation by about 20%. These simulations took roughly the same amount of computation time, but we note that as the number of neurons of the DNS increases, the population simulation becomes far more computationally efficient. Since the fluctuations in the DNS about the true solution scale inversely proportional to the square root of the number of neurons, one would need four times as many neurons to reduce the error by half. For an uncoupled population, the computation time would increase by a factor of about 4. The increase in computation time for the DNS is even greater when the neurons are coupled, whereas the population simulation demands no extra computation time.

3.1 An Exactly Solvable Case. To compare the results of the population simulation with an exactly solvable problem, we first considered the case of constant driving, $\sigma^0\epsilon = \frac{I}{C}$, in the diffusion approximation 2.22 of the population equation. We further suppose that the diffusive term, $\frac{\sigma^0\epsilon^2}{2}\frac{\partial^2\rho}{\partial V^2}$, is negligible, a justifiable simplification if the voltage increment ϵ arising from a random spike input is small but $\sigma^0\epsilon$ finite. This case, which may also be viewed as a population model for which the external driving is noiseless, then reduces to the pure advection equation,

$$\frac{\partial\rho}{\partial t} = -\frac{\partial\left((F^V + \frac{I}{C})\rho\right)}{\partial V} - \frac{\partial(F^h\rho)}{\partial h} + \delta(V - V_r)\, J^V(V_\theta, h, t). \tag{3.1}$$

Here $\mathbf{F} = \left(F^V, F^h\right)$ is defined by equation 2.10. This equation can be solved exactly by the method of characteristics.

In the absence of diffusive smearing of the density field by stochastic effects, the population density ρ traces the single-neuron orbit defined by equations 2.1 and 2.5. Upon dividing these equations, we obtain the characteristic trace equation,

$$\frac{dV}{dh} = \frac{F^V + \frac{I}{C}}{F^h}. \tag{3.2}$$

Integrating equation 3.2 in the Ca^{2+}-inactivated region ($V > V_h$) gives

$$\begin{aligned} V = \frac{1}{C}e^{\gamma_T(h-h_0)}\Bigg[& CV_0\left(\frac{h}{h_0}\right)^{\gamma_L} + \tau_h^-(I + g_L V_L)(\gamma_T)^{\gamma_L} \\ & \times(\Gamma(-\gamma_L, \gamma_T h) - \Gamma(-\gamma_L, \gamma_T h_0)) \\ & + CV_T(\gamma_T h)^{\gamma_L} e^{\gamma_T h_0}(\Gamma(1-\gamma_L, \gamma_T h) - \Gamma(1-\gamma_L, \gamma_T h_0))\Bigg] \end{aligned} \tag{3.3}$$

where $\gamma_T = \frac{g_T\tau_h^-}{C}, \gamma_L = \frac{g_L\tau_h^-}{C}, \Gamma(a, z) = \int_z^\infty t^{a-1}e^{-t}\,dt$ is the incomplete gamma function (Abramowitz & Stegun, 1972), h_0 defines the starting point of a

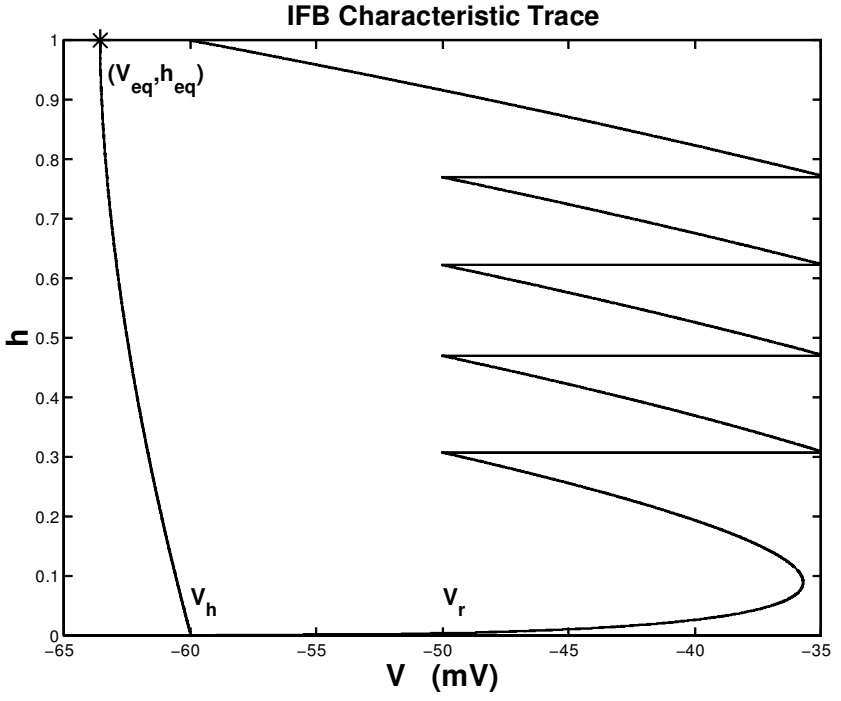

Figure 2: Characteristic traces (see equations 3.3 and 3.4) with an input current $I = .05\ \frac{\mu A}{cm^2}$, which leads to a burst of four spikes. The asterisk in the upper left corner at $(V_{eq}, h_{eq}) = (-63.6, 1)$ indicates the fixed point to which the neuron will eventually settle. The reset condition has been added manually.

particular characteristic curve, and $V_0 = V(h_0)$. In the Ca^{2+}-deinactivated region, the dynamics of V and h are uncoupled, and we find

$$V = V_L + \frac{I}{g_L} + \left[V_0 - V_L - \frac{I}{g_L}\right]\left(\frac{h-1}{h_0-1}\right)^{\frac{g_L \tau_h^+}{C}}. \tag{3.4}$$

Characteristic lines for the case of a calcium-driven burst event, using the initial point $(V_0, h_0) = (V_h, 1)$, are shown in Figure 2. Because the input is nonstochastic and subthreshold, a neuron driven with this small current $(I = .05\ \frac{\mu A}{cm^2})$ equilibrates at the fixed point at $(V_{eq}, h_{eq}) = (-63.6, 1)$ (marked by the asterisk). Before reaching the equilibrium, a burst of four spikes, preceded by a low-threshold calcium spike, was fired before the calcium channels fully deinactivated. Stochastic input, explored in section 3.2, has the effect of increasing the average firing rate of a population of IFB cells due to additional depolarizing input from random, excitatory spike inputs.

However, the number of spikes per burst event generally remains the same because the IFB dynamics are dominated by the calcium current when $V > V_h$ and $h > 0$ (see Figure 5 for comparison).

If the input current is large, each neuron fires in a classic integrate-and-fire (Omurtag, Knight, and Sirovich, 2000) tonic mode and the calcium channel equilibrates to the inactivated state $h = 0$. In this case, the equilibrium potential, V_{eq}, of the average cell is given by setting $\frac{dV}{dt} = 0$ in equation 2.1, with the result

$$V_{eq} = \frac{I}{g_L} + V_L. \tag{3.5}$$

The population is driven past threshold when $I > I_{crit} = g_L(V_\theta - V_L)$, in which case each neuron of the population fires a periodic train of spikes with a time-averaged firing rate that eventually equilibrates to a constant value $\bar{r}$,

$$\bar{r} = \frac{1}{T}\int_{t-T}^{T} r(s)\, ds\,, \tag{3.6}$$

with $r(t)$ given by

$$r(t) = \int_0^1 dh\, F^V(V_\theta, h)\rho(V_\theta, h, t)\,. \tag{3.7}$$

This time-averaged firing rate $\bar{r}$ is independent of the reference time, t, provided t is chosen large enough for each member of the population to have equilibrated to its limit cycle. The interval T is chosen large enough to encompass many traversals of a given cell from its reset potential through the threshold. To test the accuracy of the population simulation, we compared time-averaged population firing rate, $\bar{r}$, with the single-neuron firing rate, $f(I)$, which is obtained from equation 2.1 upon integrating through the interval $[V_r, V_\theta]$:

$$f(I) = \left[\frac{C}{g_L}\ln\frac{V_r - V_L - I/g_L}{V_\theta - V_L - I/g_L}\right]^{-1}. \tag{3.8}$$

In Figure 3 we plot the exact result (see equation 3.8) and simulation results, and see that they are in excellent agreement.

3.2 Constant Stochastic Input. Irregularity in the arrival times in the external driving introduces stochasticity into the population evolution, which is modeled either as diffusion (see equation 2.22) or finite jumps in the membrane voltage (see equation 2.12). In either case, there is a finite chance that a cell will be driven through the threshold, V_θ, even if the mean current

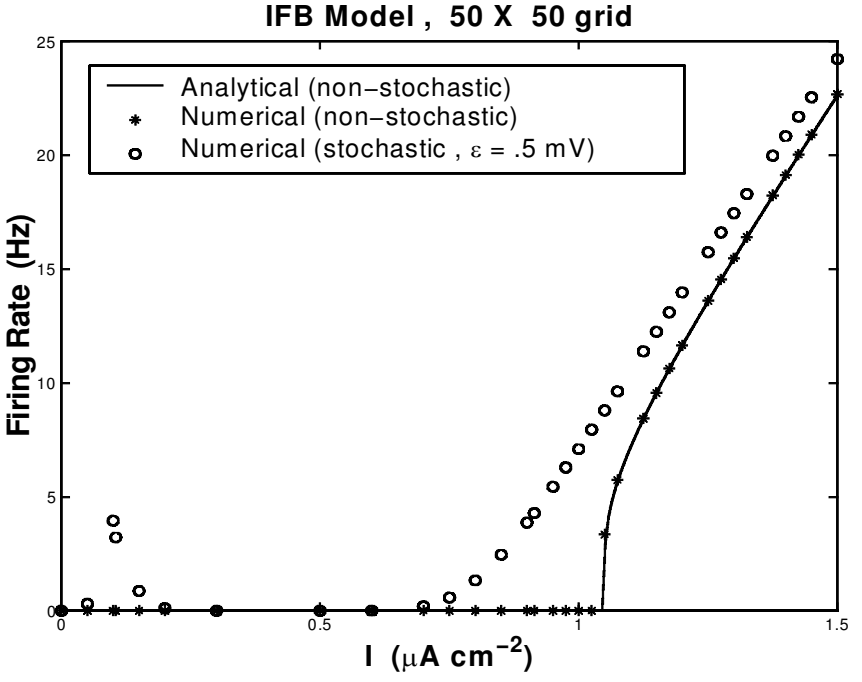

Figure 3: Comparison of the exact analytical firing rate (see equation 3.8) (solid line) for a neuron driven by a nonstochastic current with the population firing rate obtained from simulation (asterisks). The population firing rate of the finite-jump model with stochastic driving ($\epsilon = .5$ mV) at an equivalent Poisson rate is included for comparison (circles). Horizontal axis: Applied current I ($\frac{\mu A}{cm^2}$). Vertical axis: Firing rate $r(t)$ (Hz).

is not strong enough to push the average cell through threshold. Thus, we expect to see higher firing rates compared to the case of purely deterministic driving (see section 3.1). The population results are in accord with this expectation, as shown in Figure 3.

A notable feature of stochastic input is a nonvanishing firing rate for driving currents below the threshold. In Figure 3, this effect appears in the equilibrium firing-rate curve as a bump peaked at $I = .175\ \frac{\mu A}{cm^2}$ for the parameter values stated in Table 1. This bump is a consequence of low-threshold calcium spiking events. If the cell's resting potential lies near the calcium channel activation threshold, $V_{eq} \approx V_h$, which occurs if the input rate satisfies $\sigma^0 \approx \frac{g_L(V_h - V_L)}{C\epsilon}$ $\left(\sigma^0 \approx .0875\ \text{ms}^{-1}\right)$, then random walks in voltage, in cooperation with activated calcium currents, occasionally drive neurons

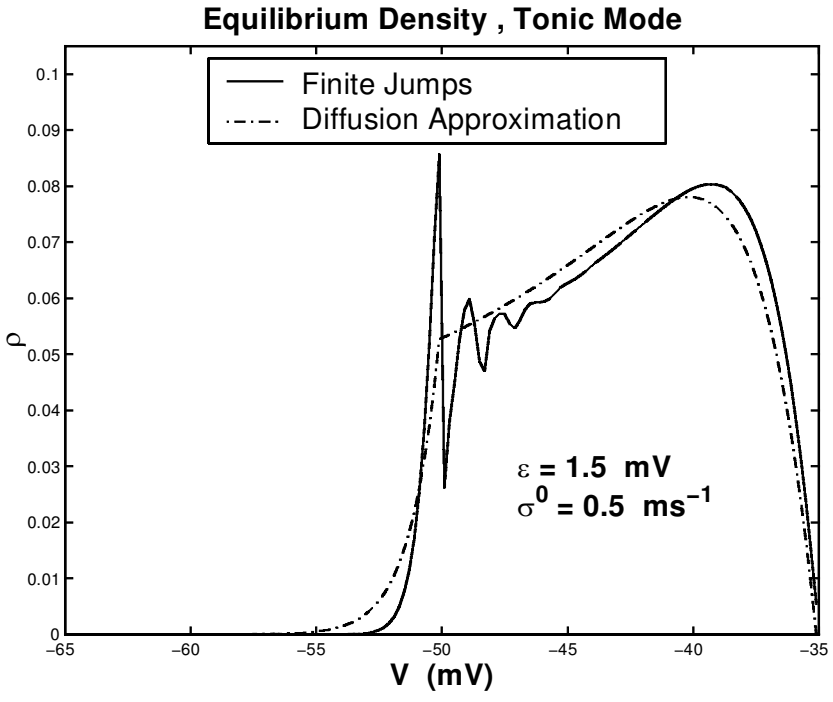

Figure 4: Comparison of the time-independent equilibrium distributions for a population firing in tonic mode. The figure is plotted in the $h = 0$ plane. Solid line: Finite-jump numerical solution. Dash-dot line: Diffusion approximation. The numerically generated distribution, equation 2.22, and the analytical solution, equation 3.9, for the diffusion approximation are imperceptibly different. Parameters: $\sigma^0 = .5\,\mathrm{ms}^{-1}$, $\epsilon = 1.5\,\mathrm{mV}$, 150 grid points in V and h (all other parameters given by Table 1).

through the threshold V_θ. If the average resting membrane potential lies too far above V_h but still well below the threshold, then the calcium currents are rarely deinactivated for a sufficient duration to trigger the low-threshold calcium spike.

With a fixed Poisson arrival rate, the population always achieves a time-independent equilibrium whose characteristic features hinge on whether the population is firing in tonic or burst mode. The tonic mode for any individual LGN cell is typified by an uninterrupted sequence of independently generated spikes, all occurring in the calcium-inactivated state (McCormick & Feeser, 1990). The equilibrium profile for a tonic-spiking population thus lies in a plane cutting through $h = 0$ in the two-dimensional phase space (see Figure 4). By contrast, a cell in burst mode fires clusters of calcium-triggered

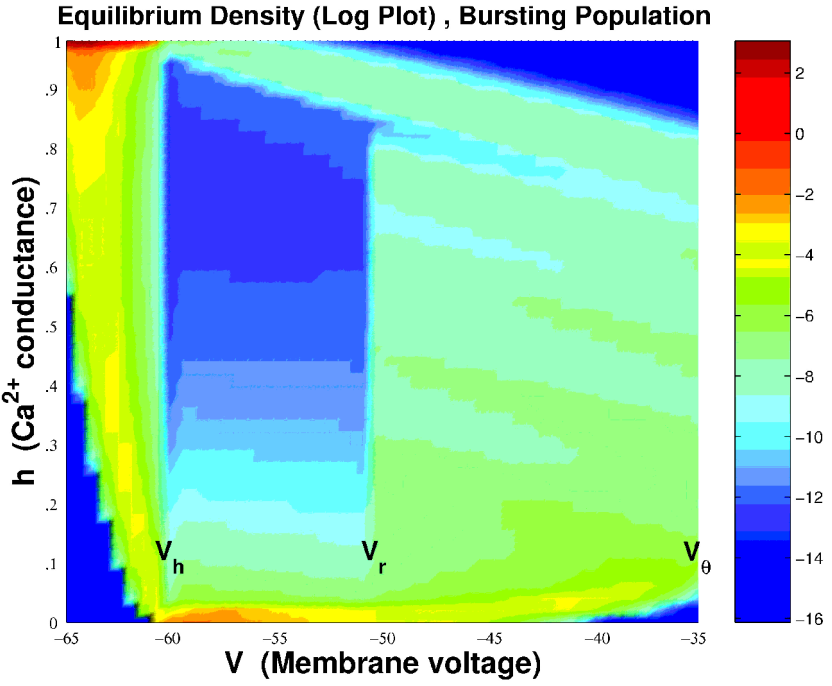

Figure 5: Density plot of the numerically generated equilibrium solution for a population of continuously bursting cells ($\log \rho$ is plotted in the $V - h$ plane with color scale indicated on the right). Parameters: 50×50 grid resolution, $\epsilon = 1\,\text{mV}$, $\sigma^0 = .025\,\text{ms}^{-1}$, and all other parameters as in Table 1. The more jagged features of the density distribution are numerical artifacts owing to the modest resolution.

spikes followed by a refractory period on the order of 100 ms. The burst cycle repeats provided that any depolarizing input is small enough to allow the cell to rehyperpolarize below the calcium deinactivation threshold potential. Consequently, the density profile for a repetitively bursting population is spread throughout the phase space (see Figure 5).

3.2.1 Tonic Spiking. Since tonic spiking cells have inactivated calcium currents ($h = 0$), we may obtain an analytical expression for the equilibrium solution by solving the time-independent population equation in the absence of h-dependent dynamics. For ease of comparison with the numerical results, we focus on the more analytically tractable diffusion approximation,

equation 2.22, which has the equilibrium solution

$$\rho_{eq}(V) = \frac{2CJ_\theta}{I\epsilon} e^{\beta V - \frac{\alpha}{2}V^2} \int_V^{V_\theta} e^{-\beta s + \frac{\alpha}{2}s^2} H(s - V_r)\, ds, \tag{3.9}$$

where $\alpha = \frac{2g_L}{I\epsilon}$, $\beta = \frac{2}{\epsilon}(1 + \frac{g_L V_L}{I})$, and $H(V - V_r)$ is the Heaviside function. The equilibrium firing rate, $J_\theta = J^V(V_\theta, 0, t)$, is determined self-consistently from the normalization condition, equation 2.15. The exact solution, equation 3.9, is virtually identical to the simulation result. It is also seen that the diffusion approximation, when compared to the finite-jump case, has the effect of smoothing the population distribution. The displacement of the peak toward a lower voltage occurs because the diffusion approximation, obtained by a truncated Taylor series of the density ρ, does not correctly capture the boundary layer near $V = V_\theta$ unless the input current is close to the threshold for tonic spiking. This issue, and others related to the equilibrium profile for a population of integrate-and-fire neurons, has been explored more extensively in Sirovich et al. (2000).

3.2.2 Burst Firing. For the population to exhibit continuous bursting under statistically steady input, the driving must be small enough so that the average neuron spends most of its time sufficiently hyperpolarized below (or near) the Ca^{2+} activation threshold at $V = V_h$. This situation is achieved when the input spike rate satisfies $\sigma^0 < \frac{g_L}{C\epsilon}(V_h - V_L)$.

The representative features of a population in burst mode are illustrated in Figure 5, which shows a numerical simulation of the population equation, 2.19, driven by random, finite voltage jumps. Most of the neuron density equilibrates near the fixed point $(V_{eq}, h_{eq}) = (-63.6, 1)$ of the single-neuron system under the driving condition of the same average current, but steady instead of in jumps. Thus, in Figure 5, one sees the majority of neurons residing in the upper-leftmost portion of the phase space, with deinactivated calcium currents ($h = 1$) but not quite enough input to push them forward through the activation threshold very often. However, because the input is noisy, some cells may randomly walk past V_h. This is reflected in the equilibrium profile by the faint stripes in the right half of the phase space (compare with the single-neuron orbit, driven by DC input, of Figure 2). These characteristic stripes indicate bursting cells with four spikes per burst. As Figure 5 shows, a significant number of cells, after going through a burst cycle, also temporarily get stuck in a calcium-inactivated state ($h = 0$) near the activation threshold V_h, again owing to stochastic drift.

3.3 Stepped Input Current. An experiment that probes the dynamical behavior of a neuron population involves the stimulation of cells by a step input from one contrast level to another (Mukherjee & Kaplan, 1995). Such experiments give insight into the approach to equilibrium and the degree of

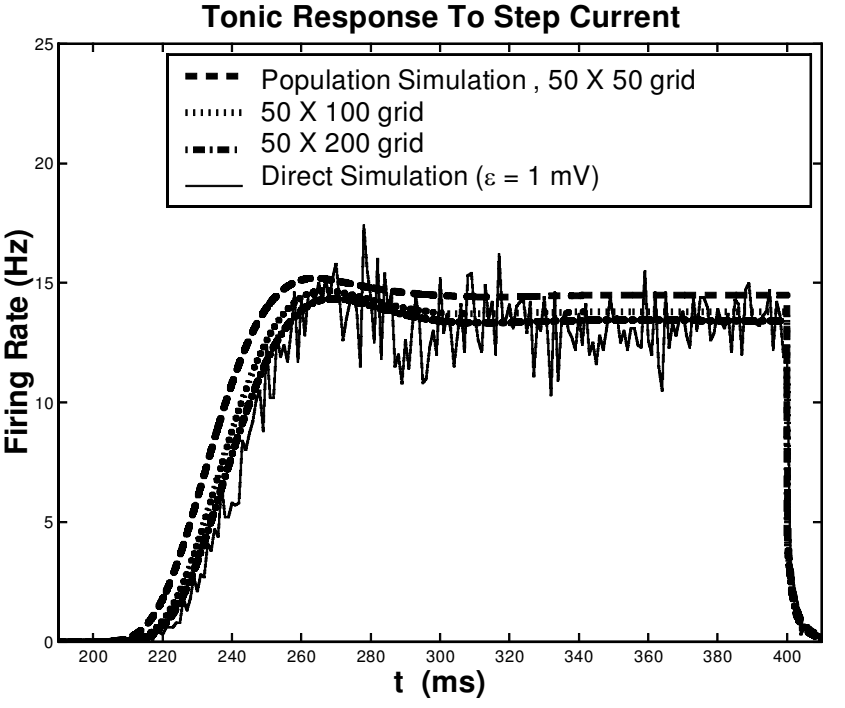

Figure 6: Firing-rate comparison of the direct simulation (solid jagged curve) with population dynamics simulations (dashed and dotted curves) at various grid resolutions in h for a mean current step from $I = .4$ to $I = 1.2\,\frac{\mu A}{cm^2}$. The step increase began at $t = 200\,\text{ms}$ and terminated at $t = 400\,\text{ms}$.

nonlinear response under various changes in contrast. For LGN neurons, it is of particular interest to understand the connection between the stimulus, or the absence of one, and the extent to which visual input is faithfully tracked by relay cell activity and sent forth to the cortex. In this section, we examine the firing activity one might observe in such an experiment for a population of LGN cells. The input is stochastic, with a mean driving rate σ^0 that steps from one constant value to another. The population dynamics for this sort of input to integrate-and-fire cells operating in tonic mode has been explored in Knight et. al (2000).

3.3.1 Current Step Between Two Calcium Inactivated States. Figure 6 compares the results of a direct numerical simulation with the IFB population model for a mean current step from $I = .4$ to $I = 1.2\,\frac{\mu A}{cm^2}$ (the mean input rate steps from $\sigma^0 = .2\,\text{ms}^{-1}$ to $\sigma^0 = .6\,\text{ms}^{-1}$). In this case, the prestep

equilibrium potential of the average neuron is $V_{eq} \approx -53.6$ mV, which lies several millivolts above the threshold V_h at which the calcium current is deinactivated. Once the current jumps to 1.2 $\frac{\mu A}{cm^2}$, the neurons fire in tonic mode since the associated equilibrium $V_{eq} \approx -30.7$ mV is well above the sodium spiking threshold, $V_\theta = -35$ mV.

The response to a range of step input that does not promote burst firing is primarily linear. Upon activation of the step at $t = 200$ ms and after a delay of about 30 ms while the membrane potential moves toward threshold, the firing rate $r(t)$ mimics the input with a step response, aside from a minor overshoot at the peak firing rate. The linearity of the input-output relationship of the tonic mode was verified by a spectral analysis; the transfer function was approximately constant, with only slight deviations at lower frequencies.

Further simulations at various input levels revealed that although the input-output relation was not exactly linear, it was far more so than when the population fired in burst mode (as discussed below). The three curves generated by the population simulation correspond to varying grid resolution in the calcium coordinate h. The population model and the DNS achieve increasing agreement as the resolution of the population simulation is increased. The reason that the equilibrated firing rate of the population model lies slightly above the mean of the DNS is attributable to finite grid effects, which are further discussed in the appendix.

3.3.2 Current Step from Calcium Deinactivated State to Calcium Inactivated State. In Figure 7 is a comparison of the firing rates of the population model at various resolutions with the DNS for a current step from $I = .1$ $\frac{\mu A}{cm^2}$ to $I = 1.33$. These current values correspond to an equilibrium potential before the step of $V_{eq} \approx -62.1$ mV (in the absence of Ca^{2+} dynamics), so the calcium channels are initially deinactivated, and a poststep equilibrium potential of $V_{eq} = -27$ mV, which is well above the firing threshold. Compared to the previous case, one expects much higher firing rates at the onset of the current step because a large fraction of cells are poised to burst. This is indeed reflected in the sharper firing-rate peak at the current jump, relative to the equilibrium firing rate to which the population relaxes (compare with Figure 6). Consistent with physiological experiments and analysis of temporal modulation transfer functions (Mukherjee & Kaplan, 1995), the bursting LGN cells in the IFB population nonlinearly modify retinal input and pass to the visual cortex a significantly altered rendition of the stimulus. Numerical simulations at different input levels, all corresponding to the burst mode, verified that the transfer function was not constant in each case. This behavior of the population activity reflects that of the single-neuron IFB model, which Smith et al. (2000) have explored quantitatively for sinusoidal input; we refer to their work for the details.

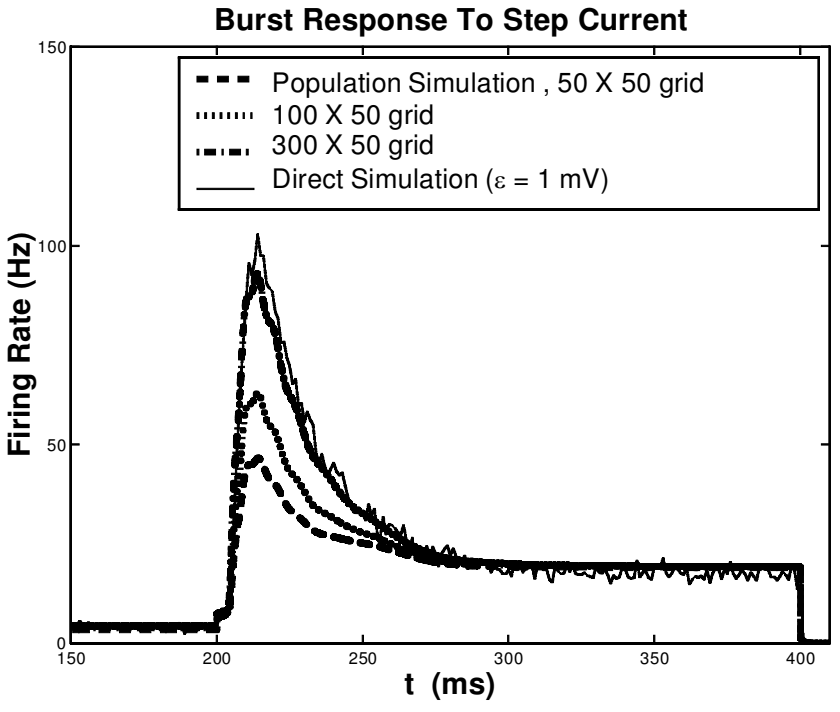

Figure 7: Firing-rate comparison of the direct simulation (solid jagged curve) with the IFB population model (dashed and dotted curves) at various grid resolutions in V for a current step from $I = .1\ \frac{\mu A}{cm^2}$ to $I = 1.33$. The onset of the step occurred at $t = 200$ ms.

It is interesting to note that the agreement between the DNS and the population simulation is less favorable for coarse grid resolutions (50 grid-points in both V and h) than in Figure 6. This is a consequence of finite grid influences that cause some of the population to drift spuriously through the calcium activation transition at V_h, an effect that is much more manifest whenever the equilibrium potential of a typical neuron in the population initially lies near V_h. This issue is elaborated on in the appendix.

Figure 8 demonstrates the increase in accuracy when the prestep voltage equilibrium is well removed from V_h. Here, the input was a current step from $I = 0\ \frac{\mu A}{cm^2}$ to $I = 1.33$, corresponding to a prestep equilibrium point $(V_{eq}, h_{eq}) = (V_L, 1)$ with $I = 0$. The neurons initially equilibrate in the upper-left corner of the phase space, far enough away from V_h to preclude significant finite-grid-influenced drift through the Ca^{2+} activation threshold. As in Figure 6, the agreement between the direct simulation and the population result is excellent at a moderate resolution.

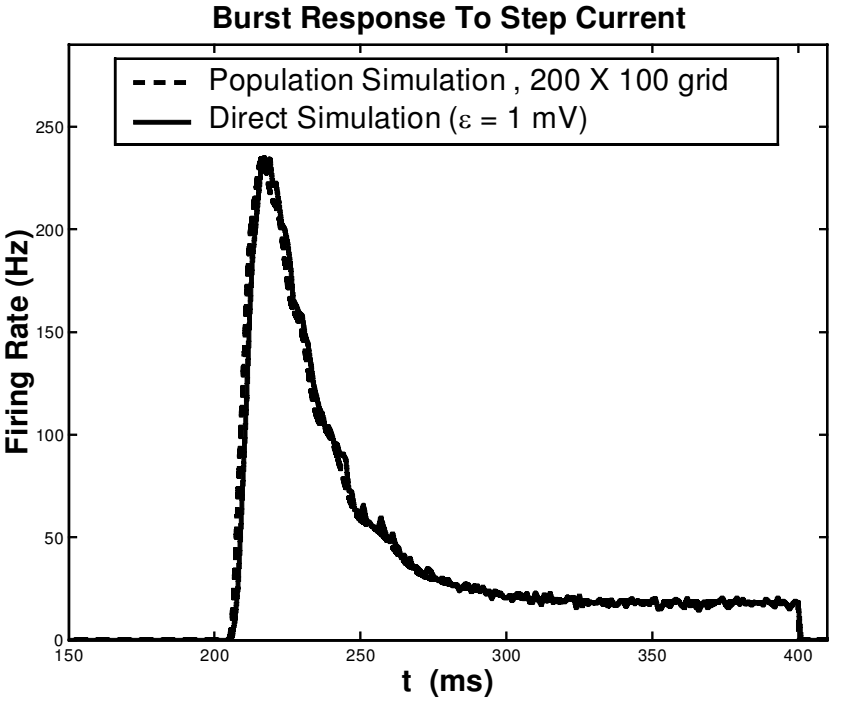

Figure 8: Comparison of firing rates for a step current from $I = 0 \frac{\mu A}{cm^2}$ to 1.33. Solid curve: Direct simulation with $\epsilon = 1$ mV. Dashed curve: Population dynamics simulation on a 200×100 grid.

4 Discussion

To capture the dynamical range of LGN cells that may fire in a burst or tonic mode, a neuron model of two or more state variables is required, since at least two fundamental timescales comprise the intrinsic dynamics of the burst mode: the relatively long interval between bursts (around 100 ms) and the short interspike interval (about 4 ms) of sodium action potentials that ride the low-threshold calcium spike. Using the single-cell IFB model of Smith et al. (2000) as a springboard, this work presents the first simulation of a population equation with a two-dimensional phase space. Most previous studies using the population method focused on the single state-space variable integrate-and-fire model (Knight, 1972; Knight et al., 1996, 2000; Nykamp & Tranchina, 2000; Omurtag, Knight, and Sirovich, 2000; Sirovich et al., 2000). Here, the computationally efficient simulations of an LGN population under a variety of stimulus conditions were seen to be in excellent agreement with direct numerical simulations of an analogous discrete net-

work (see Figures 3, 6, 7, and 8), as well as with special analytical solutions (see Figures 3 and 4).

Although the role of the intrinsic variability of LGN cells in visual processing is still unknown, a large body of experimental evidence indicates that the dual response mode—burst or tonic—has a significant effect on the faithfulness with which a retinal stimulus is transmitted to cortex. This fact may be related to attentional demands. In alert animals, the burst mode, being a more nonlinear response, could serve the purpose of signaling sudden changes in stimulus conditions (Guido & Weyand, 1995; Sherman, 1996). The tonic mode, a nearly linear response mode, presumably takes over when the cortex demands transmission of the details.

The population model of IFB neurons mirrors these qualitative features of the dual response modes. For a population initially hyperpolarized below V_h, where calcium channels are deinactivated, the response to a step input was large and nonlinear (see Figures 7 and 8). When the population was initialized with inactivated calcium currents at membrane potentials above V_h, the firing-rate response tracked the stimulus much more faithfully, indicating a primarily linear response (which a spectral analysis verifies explicitly). Further, an initially hyperpolarized IFB population driven by a large current ($I > 1.05 \frac{\mu A}{cm^2}$ for the parameters of Table 1) will fire a burst of calcium-activated spikes and then settle into a tonic firing mode. This is consistent with the experiment of Guido and Weyand (1995), in which relay cells of an awake cat fired in burst mode at stimulus onset during the early fixation phase and then switched to a tonic firing pattern thereafter. The IFB model, being of low dimension, thus shows great promise as an efficient means of simulating realistic LGN activity in models of the visual pathway.

Previous simulations of the early stages of visual processing (retina $\rightarrow$ LGN $\rightarrow$ $V1$) typically did not incorporate LGN dynamics (however, see Tiesinga & José, 2000). Typically, the LGN input used is a convolved version of the retinal stimulus, which is then relayed to the cortex (McLaughlin, Shapley, Shelley, & Wielaard, 2000; Nykamp & Tranchina, 2000; Omurtag, Kaplan, Knight, & Sirovich, 2000; Somers, Nelson, & Sur, 1995). In such simulations, no account is made of the intrinsic variability of the LGN cells or the effects of feedback from the cortex or other areas. Because the convolution of retinal input with a filter is a linear operation, most models effectively simulate LGN cells in their tonic mode. Yet the burst response mode of relay cells is certainly an important feature of LGN cells whatever the arousal level of the animal in question. Although this may be of less concern in feedforward models used to study orientation tuning in $V1$, for instance, it is a necessary consideration of any model of cortical activity when stimulus conditions promote strong hyperpolarization for significant durations, which may arise realistically from variable levels of alertness, or for simulations in which the stimulus is weak.

A dynamically faithful model of relay cell activity, dictated by experiment, is likely needed to assess the role of the massive feedback connections on the cortico-thalamic pathway. There is some evidence that feedback from a layer 6 neuron in $V1$ to the LGN may play a role in orientation tuning by synchronizing the spiking of relay cells within its receptive field (Sillito, Jones, Gerstein, & West, 1994). This suggests the possibility that cortical cells provide very specific afferent connections to reinforce the activity of the LGN neurons that excited them in the first place. Anatomical support for this has been provided by the experiments of Murphy, Duckett, and Sillito (1999), who observed that the corticofugal axons, though sparse, exhibit localized clustering of their boutons into elongated anatomical "hot spots" that synapse upon a relatively large number of target cells in the LGN and reticular nucleus. They also demonstrated a high correlation between the major axis of the elongated array of boutons and the orientation preference of the cortical cells from which they originated.

A plausible conjecture is that the cortico-thalamic feedback serves the purpose of enhancing the response of salient features such as edge orientations in the retinal input. If so, then a more dynamically realistic LGN model than those used to date is called for. In any event, the relative importance of feedback to the LGN, as opposed to intracortical connectivity and feedforward convergence, say, in the tuning of cortical cells to various modalities such as orientation and spatial frequency, is an important issue.

Future work with the population method is underway to simulate a simplified version of the thalamocortical loop, with realistic dynamical models for the LGN, layers 4 and 6 of the primary visual cortex, and the inhibitory interneurons of the thalamic reticular nucleus. The aim will be to study the functional nature of the circuitry that connects the various levels of the early visual pathway and investigate in particular the role that feedback plays in visual pattern analysis.

Appendix: Numerical Methods

A.1 Direct Simulation. The state variable $\mathbf{v} = (V, h)$ for each cell in the network is governed by the ordinary differential equation (ODE),

$$\frac{d\mathbf{v}}{dt} = \mathbf{F}(\mathbf{v}) + \hat{\mathbf{e}}_V \epsilon \sum_k \delta(t - t_k), \tag{A.1}$$

where $\hat{\mathbf{e}}_V$ is the unit vector in the V direction and $\mathbf{F}(\mathbf{v})$ is defined by equation 2.10.

The solution that corresponds to the streaming motion alone, $d\mathbf{v}/dt = \mathbf{F}(\mathbf{v}) \equiv (F^V(v, h), F^h(v, h))$, is formally denoted by the time evolution operator $e^{Q^{(1)}(t)}$:

$$\mathbf{v}(t) = e^{Q^{(1)}(t)}\mathbf{v}(0). \tag{A.2}$$

The solution that corresponds to the synaptic input alone similarly can be written as

$$\mathbf{v}(t) = e^{Q^{(2)}(t)}\mathbf{v}(0)\,. \tag{A.3}$$

Equation A.3 has a simple, explicit form for the case of fixed finite jumps:

$$e^{Q^{(2)}(t)}\mathbf{v}(0) = \mathbf{v}(0)+\epsilon n(t)\,. \tag{A.4}$$

Here, $n(t)$ is the number of impulses that have arrived during time t. It is an integer chosen randomly from the nth Poisson distribution, $P_n(t) = (\sigma t)^n e^{-\sigma t}/n!$, with mean arrival rate σ.

We are interested in solutions of the form

$$\mathbf{v}(t) = e^{(Q^{(1)}(t)+Q^{(2)}(t))}\mathbf{v}(0)\,. \tag{A.5}$$

According to the Baker-Campbell-Hausdorff lemma (Sakurai, 1994), a second-order accurate splitting of the exponential operator, equation A.5, is

$$\mathbf{v}(t+\Delta t) = e^{Q^{(1)}(\Delta t/2)}e^{Q^{(2)}(\Delta t)}e^{Q^{(1)}(\Delta t/2)}\mathbf{v}(t)+O(\Delta t^3)\,. \tag{A.6}$$

We use a second-order Runge-Kutta method for the streaming operator $e^{Q^{(1)}}$. Thus, the above operator splitting method provides an efficient second-order accurate numerical scheme for integrating equation A.1. However, the streaming direction field of the IFB neuron contains discontinuous changes in the voltage variable V due to the Heaviside calcium-channel activation function, equation 2.4, and the pointwise (in h) reset condition. We now describe how we handle these discontinuities numerically with the same second-order accuracy.

Suppose the discontinuity occurs when $v = v_d$. After a time step Δt, if v_d is found to lie between $v(t)$ and $v(t+\Delta t)$, then the integration is performed from the current state up to the discontinuity. Let the state at time t be denoted (v, h). Define $\overline{v} = \frac{1}{2}(v_d + v)$, and let $\overline{\Delta t}$ denote the time it takes to move from the present state (v, h) to the state $(\overline{v}, \overline{h})$, which lies between the present state and the point where the trajectory crosses the discontinuity, (v_d, h_*). The time to reach the discontinuity is Δt_*. By Taylor expanding the direction field at (v, h) we find

$$\overline{\Delta t} = \frac{\overline{v}-v}{F^V(v,h)} + O(\Delta t^2)\,. \tag{A.7}$$

We remark that $F^V(v, h) = 0$ almost never occurs in the phase plane for the cases of interest. The solution for the calcium channel ODE, equation 2.5, is then written

$$\overline{h} = e^{Q_h^{(2)}(\overline{\Delta t})}h = e^{Q_h^{(2)}\left(\frac{1}{2}(v_d-v)/F^V(v,h)\right)}h + O(\Delta t^2)\,. \tag{A.8}$$

Next, after the direction field is Taylor expanded about $(\overline{v}, \overline{h})$, one can show that

$$v_d = v + F^V(\overline{v}, \overline{h})\Delta t_* + O(\Delta t^3)\,, \tag{A.9}$$

whence

$$\Delta t_* = \frac{v_d - v}{F^V\left(\frac{1}{2}(v_d + v), e^{Q_h^{(2)}\left(\frac{1}{2}(v_d - v)/F^V(v,h)\right)}h\right)} + O(\Delta t^3)\,. \tag{A.10}$$

Consequently, the point where the trajectory crosses the discontinuity is found to be

$$(v_d, h_*) = (v_d, e^{Q_h^{(2)}(\Delta t_*)}h + O(\Delta t^3)). \tag{A.11}$$

A.2 Population Simulation. Equation 2.7 is linear in ρ. However, due to the boundary conditions in the V-direction (population exiting the phase space at threshold resurfaces in the middle of the grid) and the tendency of the population to pile up at $h = 0$ and $h = 1$, it is necessary to use relatively sophisticated methods to integrate the equations. In particular, if we simply discretize the grid and expand the derivative terms to second order, oscillations due to the discretization become amplified when the population piles up at the h boundaries and population flux is reintroduced into the grid by the reset boundary condition. The oscillations then cause the population density to take on negative values in regions of the phase space. For this reason, we employed a second-order total-variation-diminishing (TVD) scheme.

The undesirable oscillations in finite difference-based schemes used to evolve advection equations may be overcome by the TVD algorithm (Hirsch, 1992). The scheme that we use for the advective term in the population equation 2.12 is a second-order upwind method, for which we describe here the one-dimensional version. The evolution of the conserved variable, ρ, is governed by

$$\frac{d\rho_i}{dt} = -\frac{\delta^-}{\Delta x}\left[f^{*(R)}_{i+\frac{1}{2}} + \frac{1}{2}\psi^+_{i-\frac{1}{2}}(f_i - f^{*(R)}_{i-\frac{1}{2}}) + \frac{1}{2}\psi^-_{i+\frac{3}{2}}(f_{i+1} - f^{*(R)}_{i+\frac{3}{2}})\right], \tag{A.12}$$

where an i subscript indicates the ith grid zone, $f_i = (F\rho)_i$ is a numerical approximation of the streaming flux (where F is a component of the direction field), and the difference operator $\delta^-[u_i] = u_i - u_{i-1}$. The parameters ψ^+ and ψ^- are flux limiters that are dynamically adjusted to control spurious oscillations arising from large, streaming flux gradients, which in our case occur at lines of discontinuity ($V = V_r$ and $V = V_h$) and along lines at which the population tends to pile up ($h = 0$ and $h = 1$). The flux limiter used was

Roe's Superbee limiter, which is defined by

$$\psi^{+}_{i-\frac{1}{2}} = \psi\left[\frac{f_{i+1} - f^{*(R)}_{i+\frac{1}{2}}}{f_i - f^{*(R)}_{i-\frac{1}{2}}}\right], \tag{A.13}$$

$$\psi^{-}_{i+\frac{3}{2}} = \psi\left[\frac{f_i - f^{*(R)}_{i+\frac{1}{2}}}{f_{i+1} - f^{*(R)}_{i+\frac{3}{2}}}\right], \tag{A.14}$$

$$\psi[r] = \max[0, \min(2r, 1), \min(r, 2)], \tag{A.15}$$

where the first-order Roe flux is defined as

$$f^{*(R)}_{i+\frac{1}{2}} = \frac{1}{2}(f_i + f_{i+1}) - \frac{1}{2}\left|a_{i+\frac{1}{2}}\right|(\rho_{i+1} - \rho_i) \tag{A.16}$$

$$a_{i+\frac{1}{2}} = \frac{1}{2}(F_i + F_{i+1}). \tag{A.17}$$

This method eliminates undesirable oscillations due to discretization and reduces negative densities to values on the order of the numerical round-off error. We found one undesirable feature with this method. If the direction field points in opposite directions between grid points n and $n + 1$, the populations on either side diverge, one tending to ∞ and the other to $-\infty$. To cure this problem, we set the Roe flux, equation A.16, to zero at the grid boundary between grid points n and $n + 1$. With this modification, the method works extremely well for the advective terms in equations 2.12 and 2.22.

The other terms of the population equation, corresponding to the stochastic input, were also discretized to second order. For the finite-jump model, equation 2.12, the source term $\sigma(t)\rho(V - \epsilon h, t)$ was discretized by linear interpolation. The diffusion term in the diffusion approximation, equation 2.22, was discretized by a second-order central difference.

A.3 Discrepancies Between the Direct Simulation and the Population Simulation. We commented in section 3.3 that the accuracy of the population simulation with a step input current is sensitive to the prestep voltage equilibrium of the neuron. In Figure 7, for example, we noted that a fine resolution (300 grid points in V) was necessary to achieve reasonable agreement in the firing rates of the direct simulation and the TVD simulation of the population equation, 2.12. For other cases in which the prejump membrane potential equilibrium was well away from V_h, we generally found that the population simulation with roughly 100 grid points in each direc-

tion converged to a direct simulation of sufficiently many neurons. We now comment on why this is so.

In cases where the prejump state of the average neuron is far away from V_h, the main source of numerical error arose from the resolution in the recovery variable h. Since all the neurons equilibrate at $h = 0$ before the current step, the TVD algorithm imposes large dissipation at the bottom boundary of the phase space in order to avoid grid-scale oscillations in the density ρ. As the grid becomes finer in the h-direction, corresponding to diminished flux limiting and less numerical dissipation, the predicted firing rates of the population model converge to that of the direct simulation (see Figure 6). Population model firing rates err slightly on the high side owing to the finite accuracy, as some neurons achieve their equilibrium at a value of h slightly larger than zero. These neurons feel a slightly larger depolarizing input, due to a nonvanishing T-channel current, and thus achieve the firing-rate threshold at the onset of the current step faster than their counterparts, which lie initially at $h = 0$.

When $V_{eq} \approx V_h$ before the current step, the TVD simulations are more sensitive to the resolution in the voltage variable. As seen in Figure 7, with a coarse resolution of 50 grid points in V, the firing rate of the population simulation is off by approximately 56% at peak firing. As the resolution is increased to 300 grid points in V, the maximal error drops to about 8%. These observations are attributable to the spurious drift of neurons through V_h owing to finite grid effects, something from which the direct simulation does not suffer. We also observed that the calculated firing rates were relatively insensitive to the resolution in h, which here was chosen to be 50 grid points.

Comparison of the equilibrium profiles in Figure 9 gives a better understanding of the firing-rate discrepancies between the direct simulation and the population dynamics simulation shown in Figure 7. In the direct simulation, stochastic voltage jumps across V_h cause some neurons to equilibrate at $h = 0$ and some at $h = 1$, as reflected in the top panel of Figure 9. Similar peaks in the density arise in the population simulation. However, as the lower panel of Figure 9 shows, many more neurons lie near $h = 0$ relative to the direct simulation. Consequently, more neurons are poised to run through a burst cycle at the onset of the step current in the direct simulation, which is why the peak firing rate associated with the bursting event is greater than that calculated in the population model. This error decreases as the $V-$direction mesh of the population code is made finer. Increases in resolution beyond 50 grid points in the h-direction did not alter the results significantly. To deal effectively with these finite grid issues, one option is to employ a variable phase-space mesh that has finer resolution near points of discontinuity along the voltage axis (at V_h and V_r), and near the grid lines at $h = 0$ and $h = 1$ where the population tends to pile up. We leave such refinements to future work.

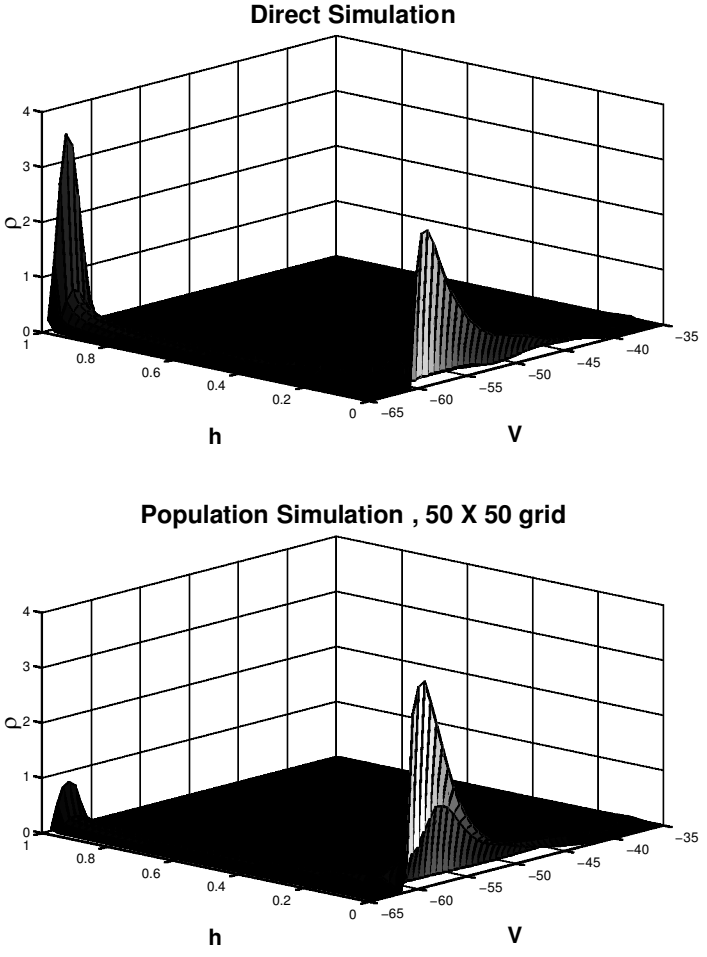

Figure 9: Equilibrium population distributions corresponding to a mean driving current $I = .1 \frac{\mu A}{cm^2}$. (Top): Direct simulation with stochastic driving (fixed jumps of size $\epsilon = 1$ mV). (Bottom): Population dynamics simulation (50×50 grid). Note that many more neurons equilibrate near $h = 0$ in the population dynamics simulation relative to that of the direct simulation.

Acknowledgments

This work has been supported by NIH/NEI EY 11276, NIH/NIMH MH50166, NIH/NEI EY01867, NIH/NEI EY9314, DARPA MDA 972-01-1-0028, and ONR N00014-96-1-0492. E. K. is the Jules and Doris Stein Research to Prevent Blindness Professor at the Ophthalmology Department at Mount Sinai.

References

Abramowitz, M. A., & Stegun, I. A. (1972). *Handbook of mathematical functions with formulas, graphs, and mathematical tables.* Washington, DC: U.S. Government Printing Office.

Guido, W., Lu, S., & Sherman, S. M. (1992). Relative contributions of burst and tonic responses to the receptive field properties of lateral geniculate neurons in the cat. *J. Neurophysiol., 68*, 2199–2211.

Guido, W., & Weyand, T. G. (1995). Burst responses in lateral geniculate neurons of the awake behaving cat. *J. Neurophysiol., 74*, 1782–1786.

Hirsch, C. (1992). *Numerical computation of internal and external flows*. New York: Wiley.

Jahnsen, H., & Llinas, R. (1982). Electrophysiology of mammalian thalamic neurons in vitro. *Nature, 297*, 406–408.

Knight, B. W. (1972). Dynamics of encoding in a population of neurons. *J. Gen. Physiol., 59*, 734–766.

Knight, B. W. (2000). Dynamics of encoding in neuron populations: Some general mathematical features. *Neural Comp., 12*, 473–518.

Knight, B. W., Manin, D., & Sirovich, L. (1996). Dynamical models of interacting neuron populations. In E. C. Gerf (Ed.), *Symposium on Robotics and Cybernetics: Computational Engineering in System Applications.* Lille, France: Cite Scientifique.

Knight, B. W., Omurtag, A., & Sirovich, L. (2000). The approach of a neuron population firing rate to a new equilibrium: An exact theoretical result. *Neural Comp., 12*, 1045–1055.

Livingstone, M. S., & Hubel, D. H. (1981). Effects of sleep and arousal on the processing of visual information in the cat. *Nature, 291*, 554–561.

McCormick, D. A., & Feeser, H. R. (1990). Functional implications of burst firing and single spike activity in lateral geniculate relay neurons. *Neurosci., 39*, 103–113.

McLaughlin, D., Shapley, R., Shelley, M., & Wielaard, D. J. (2000). A neuronal network model of macaque primary visual cortex (V1): Orientation selectivity and dynamics in the input layer 4Cα. *PNAS, 97*, 8087–8092.

Mukherjee, P., & Kaplan, E. (1995). Dynamics of neurons in the cat lateral geniculate nucleus: In vivo electrophysiology and computational modeling. *J. Neurophysiol., 74*, 1222–1243.

Mukherjee, P., & Kaplan, E. (1998). The maintained discharge of neurons in the cat lateral geniculate nucleus: Spectral analysis and computational modeling. *Vis. Neurosci., 15*, 529–539.

Murphy, P., Duckett, S., & Sillito, A. (1999). Feedback connections to the lateral geniculate nucleus and cortical response properties. *Science, 286*, 1552–1554.

Nykamp, D., & Tranchina, D. (2000). A population density approach that facilitates large-scale modeling of neural networks: Analysis and an application to orientation tuning. *J. Comp. Neurosci., 8*, 19–50.

Omurtag, A., Kaplan, E., Knight, B. W., & Sirovich, L. (2000). A population approach to cortical dynamics with an application to orientation tuning. *Network: Comput. Neural Syst., 11*, 247–260.

Omurtag, A., Knight, B. W., & Sirovich, L. (2000). On the simulation of large populations of neurons. *J. Comp. Neurosci., 8*, 51–63.
Sakurai, J. J. (1994). *Modern quantum mechanics*. Reading, MA: Addison-Wesley.
Sherman, S. M. (1996). Dual response modes in lateral geniculate neurons: Mechanisms and functions. *Vis. Neurosci., 13*, 205–213.
Sherman, S. M., & Guillery, R. W. (1996). Functional organization of thalamocortical relays. *J. Neurophysiol., 76*, 1367–1395.
Sillito, A. M., Jones, H. E., Gerstein, G. L., & West, D. C. (1994). Feature-linked synchronization of thalamic relay cell firing induced by feedback from the visual cortex. *Nature, 369*, 479–482.
Sirovich, L., Knight, B. W., & Omurtag, A. (2000). Dynamics of neuronal populations: The equilibrium solution. *SIAM J. Appl. Math., 60*, 2009–2028.
Smith, G. D., Cox, C. L., Sherman, S. W., & Rinzel, J. (2000). Fourier analysis of sinusoidally driven thalamocortical relay neurons and a minimal integrate-and-fire-or-burst model. *J. Neurophysiol., 83*, 588–610.
Somers, D. C., Nelson, S. B., & Sur, M. (1995). An emergent model of orientation selectivity in cat visual cortical simple cells. *J. Neurosci., 15*, 5448–5465.
Steriade, M., & Contreras, D. (1995). Relations between cortical and thalamic cellular events during transition from sleep patterns to paroxysmal activity. *J. Neurosci., 15*, 623–642.
Tiesinga, P.H.E., & Josè, J. V. (2000). Synchronous clusters in a noisy inhibitory neural network. *J. Comp. Neurosci., 9*, 49–65.
Troy, J. B., & Robson, J. G. (1992). Steady discharges of X and Y retinal ganglion cells of cat under photopic illuminance. *Vis. Neurosci., 9*, 535–553.
Tuckwell, H. (1988). *Introduction to theoretical neurobiology*. Cambridge: Cambridge University Press.

Received February 13, 2001; accepted August 10, 2001.